Loop-Type Wave-Generation Method for Generating Wind Waves under Long-Fetch Conditions

NAOHISA TAKAGAKI,[a] SATORU KOMORI,[b,c] MIZUKI ISHIDA,[d] KOJI IWANO,[e] RYOICHI KUROSE,[d] AND NAOYA SUZUKI[f]

[a] *Department of Mechanical Engineering, University of Hyogo, Himeji, Japan*
[b] *Research Center for Highly-Functional Nanoparticles, Doshisha University, Kyotanabe, Japan*
[c] *Center for Earth Information Science and Technology, Japan Agency for Marine-Earth Science and Technology (JAMSTEC), Yokohama, Japan*
[d] *Department of Mechanical Engineering and Science, Kyoto University, Kyoto, Japan*
[e] *Department of Mechanical Science and Engineering, Nagoya University, Nagoya, Japan*
[f] *Department of Mechanical Engineering, Faculty of Science and Engineering, Kindai University, Osaka, Japan*

(Manuscript received 20 March 2017, in final form 27 July 2017)

ABSTRACT

It is important to develop a wave-generation method for extending the fetch in laboratory experiments, because previous laboratory studies were limited to the fetch shorter than several dozen meters. A new wave-generation method is proposed for generating wind waves under long-fetch conditions in a wind-wave tank, using a programmable irregular-wave generator. This new method is named a loop-type wave-generation method (LTWGM), because the waves with wave characteristics close to the wind waves measured at the end of the tank are reproduced at the entrance of the tank by the programmable irregular-wave generator and the mechanical wave generation is repeated at the entrance in order to increase the fetch. Water-level fluctuation is measured at both normal and extremely high wind speeds using resistance-type wave gauges. The results show that, at both wind speeds, LTWGM can produce wind waves with long fetches exceeding the length of the wind-wave tank. It is observed that the spectrum of wind waves with a long fetch reproduced by a wave generator is consistent with that of pure wind-driven waves without a wave generator. The fetch laws between the significant wave height and the peak frequency are also confirmed for the wind waves under long-fetch conditions. This implies that the ideal wind waves under long-fetch conditions can be reproduced using LTWGM with the programmable irregular-wave generator.

1. Introduction

It is very important to predict the momentum, heat, and mass transfer across the air–sea interface during tropical cyclones, as the transfer mechanism has significant influence on the accuracy of the predictions of future climate change, the intensity of the tropical cyclones, and other meteorological phenomena. In particular, the air–sea momentum, heat, and mass transfer at high wind speeds is significantly affected by wave breaking, and it is therefore essential to understand the formation and shape of wind waves at high wind speeds (Takagaki et al. 2016a,b).

The previous laboratory/field experiments (e.g., Kunishi and Imasato 1966; Hawkins and Rubsam 1968) showed that the drag coefficient C_D, which represents the magnitude of momentum transfer across the sea surface, is given by

$$\tau = \rho u^{*2} = \rho C_D U_{10}{}^2, \tag{1}$$

where τ is the sea surface wind shear stress, ρ is the density of air, and u^* is the air friction velocity. The previous measurements have shown the monotonous increase of C_D with the wind speed at a height of 10 m above the sea surface U_{10} at extremely high wind speeds during tropical cyclones. In contrast, recent field measurements (Powell et al. 2003) carried out using a global positioning system sonde in a tropical cyclone have shown that C_D decreases with increasing values of U_{10} at extremely high wind speeds. In addition, recent laboratory data (Donelan et al. 2004; Takagaki et al. 2012)

Corresponding author: Naohisa Takagaki, takagaki@eng.u-hyogo.ac.jp

DOI: 10.1175/JTECH-D-17-0043.1

have also shown almost constant values of C_D at extremely high wind speeds. Takagaki et al. (2012, 2016a,b) discovered that the breaking of wind waves occurs at extremely high wind speeds and this causes C_D saturation. However, because these studies are carried out under a fetch condition of less than 10 m, wave breaking and drag saturation have not yet been observed under long-fetch conditions. In addition, it is difficult to perform field experiments in tropical cyclones, as the field experiments are risky compared to laboratory experiments in terms of preventing damage to observers and researchers.

Therefore, the purpose of this study is to develop an original technique for generating wind waves with long fetches in a laboratory for discussing the air–sea momentum and scalar transfer in the wide wind speed region, including extremely high wind speeds. The laboratory experiments in such long-fetch conditions would be helpful for modeling small-scale air–sea coupling.

2. Experiment

a. Equipment and measurement methods

A high-speed wind-wave tank (HSWWT) (cf. Takagaki et al. 2012; Iwano et al. 2013; Krall and Jähne 2014) with a glass test section 15.0 m long, 0.8 m wide, and 1.6 m high was used in the experiments (see Fig. 1). Wind waves were generated in a water tank, filled with filtered tap water, at U_{10} = 19.3, 32, and 42 m s^{-1} with 2.5% variation. Mechanical waves were generated using a programmable piston-type irregular-wave generator constructed using a wave-generating board, a servomotor (Mitsubishi Electric HC-SFS-352), a function generator (NF Corporation circuit WF1973), a wave gauge, a data recorder, and a computer. The wave-generating board was an acrylic plate with a height, width, and thickness of 0.72, 0.78, and 0.02 m, respectively. The center of the board stroke was set to be $x = -0.5$ m under the entrance slope, and the maximum stroke was 0.4 m.

A laser Doppler anemometer (Dantec Dynamics LDA) was used to measure the wind velocity fluctuation. A high-powered multiline mode argon-ion (Ar^+) laser (Lexel model 95-7; λ = 488.0, 514.5 nm) of 3-W power was used. The Ar^+ laser beam was shot through the side glass wall of the tank. Scattering particles of about 1 μm in diameter generated by a fog generator (Dantec Dynamics F2010 Plus) were fed into the airflow over the waves. The sampling frequency and sampling time were 500–5000 Hz and 240 s, respectively. The air friction velocity u^* in Eq. (1) was estimated using an eddy correlation method as $u^* = (-<u'v'>)^{1/2}$ (cf. Komori et al. 1993; Takagaki and Komori 2007), where u' and v' were the streamwise and vertical air velocity fluctuations, respectively. Here, the shear stress at the interface τ was estimated by extrapolating the measured values of the Reynolds stress $<u'v'>$ to the mean surface of z = 0 m. Under neutral stratification, the wind velocity profile over the rough boundary is expressed by a logarithmic profile:

$$U(z)/u^* = \ln(z/z_0)/\kappa, \tag{2}$$

where $U(z)$ is the wind speed at an elevation of z, and κ (= 0.4) is the von Kármán constant. From Eqs. (1) and (2), C_D has a one-to-one correspondence with the roughness length (z_0) under neutral stratification:

$$\kappa C_D^{-1/2} = \ln(z_{10}/z_0), \tag{3}$$

where z_{10} = 10 m. Therefore, we evaluated z_0, C_D, and U_{10} using Eqs. (1)–(3).

Water-level fluctuations were measured using resistance-type wave gauges (Kenek CHT4-HR60BNC). The resistance wire was placed in the water, and the electrical resistance at the instantaneous water level was recorded at 500 Hz for 600 s using a digital recorder (Sony EX-UT10). The energy of the wind waves E was estimated by integrating the spectrum of water-level fluctuations over the frequency f, where the peak frequency of the wind waves f_m was defined as the peak of the spectrum. To measure the wavelength L_S and the phase velocity C_P of significant wind waves, another wave gauge was fixed downstream at Δx = 0.02 m for $U_{10} < 30$ m s^{-1} and at Δx = 0.19 m for $U_{10} \geq 30$ m s^{-1}, where Δx was the interval between the two wave gauges. The values of C_P were estimated using the cospectra method (e.g., Mitsuyasu et al. 1979).

The measurements of velocity and water-level fluctuations were carried out at a distance of x = 5.5, 6.5, 8.5, or 11.5 m from the edge (x = 0 m) of an entrance slope plate (Fig. 1). Wave absorbers were positioned at the inlet and outlet of the test section to prevent the reflection of surface waves.

b. LTWGM

Spectral models proposed for normal wind speeds (e.g., Phillips 1958; Pierson and Moskowitz 1964; Hasselmann et al. 1973; Toba 1973) are not appropriate for the generation of wind waves at extremely high wind speeds, as the wind-wave properties thereof are not well known. Therefore, a new method, referred to as the loop-type wave-generation method (LTWGM), was employed to generate waves under long-fetch conditions in HSWWT (see Fig. 1b). The LTWGM was used to extend the actual

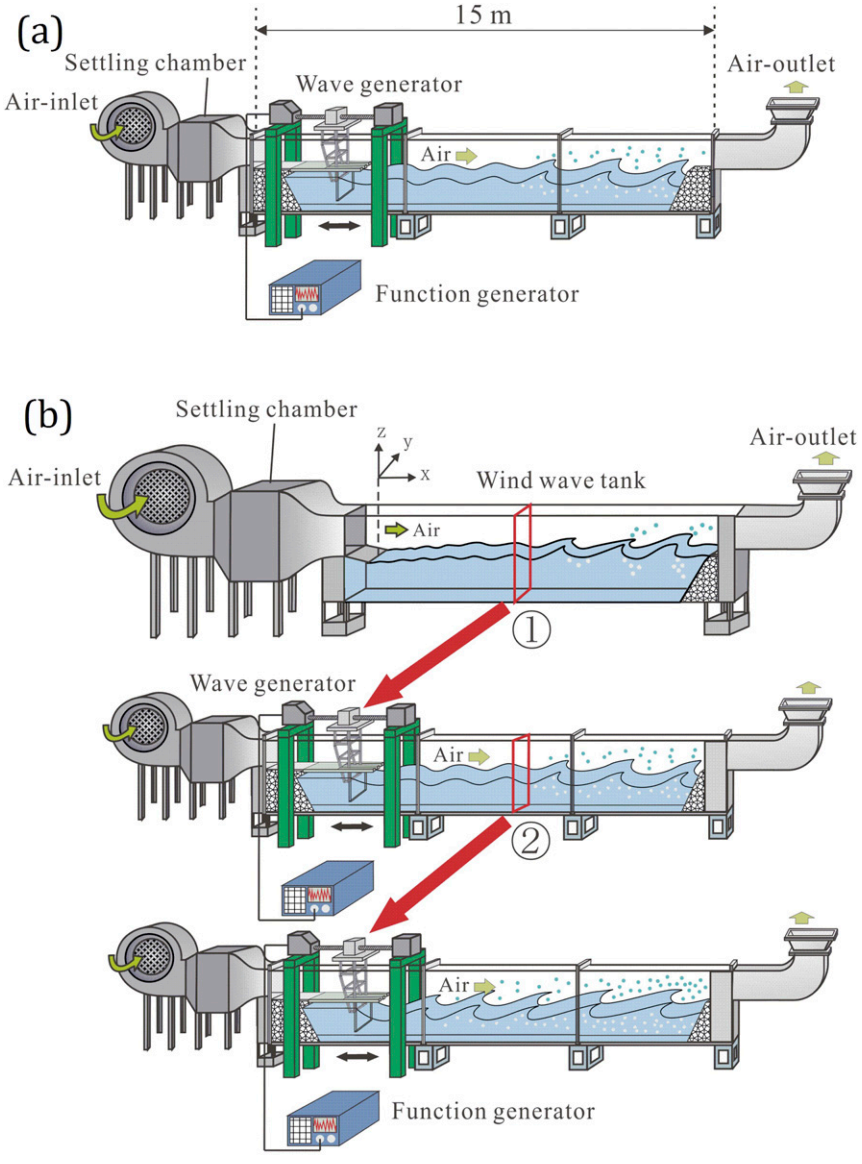

FIG. 1. (a) Schematic diagram of HSWWT and programmable irregular-wave generator, and (b) LTWGM: (top) first wind waves generated by the fan; (middle) second wind waves generated by the wave generator and fan, and the first wind-wave record; and (bottom) third wind waves generated by the wave generator and fan, and the second wind-wave record.

fetch incrementally. First, wind waves were generated using a fan without the mechanical irregular-wave generator, and the water-level fluctuation was measured at $X_{\text{loop}} = 11.5$ m (see Figs. 1b, top; Table 1). The measured spectrum at $X_{\text{initial}} = 11.5$ m was used as input (see Table 1) for the irregular-wave generator positioned at the inlet of the test section (see Fig. 1b, middle). Then, irregular wind waves were generated mechanically and forced with the fan starting at a fetch of 11.5 m and measured at 17 m ($F = X_{\text{initial}} + X_{\text{measure}} = 11.5 + 5.5 = 17$ m, where X_{measure} means the measurement location of waves for wave analysis; see Table 1). This iterative procedure was repeated to generate wind waves at different values of F (Fig. 1b, bottom). Wind waves were generated at $F = 6.5$, 17, 25.5, 34, and 42.5 m using LTWGM 0, 1, 2, 3, and 4 times, respectively. The measurement locations are listed in Table 1. In this study, the conditions with $F = 6.5$ m and $F > 6.5$ m are referred to as short- and long-fetch conditions, respectively, for distinguishing pure wind-driven waves with a short fetch from the wind waves with a long fetch generated by LTWGM. As the maximum L_S in HSWWT is approximately 1.22 m, the ratio (D/L_S)

TABLE 1. Measurement conditions: U_{10}: wind speed at a height of 10 m above the sea surface, C_D: drag coefficient, N: number of loops, F: fetch ($=X_{\text{initial}} + X_{\text{measure}}$), X_{initial}: extended length for LTWGM, X_{measure}: measurement location of waves for wave analysis this time, X_{loop}: measurement location of waves for LTWGM next time.

U_{10} (m s^{-1})	C_D ($\times 10^{-3}$)	N (—)	F (m)	X_{initial} (m)	X_{measure} (m)	X_{loop} (m)
19.3	1.76	0	6.5	—	6.5	11.5
		1	17	11.5	5.5	8.5
		2	25.5	11.5 + 8.5	5.5	8.5
		3	34	11.5 + 8.5 + 8.5	5.5	8.5
		4	42.5	11.5 + 8.5 + 8.5 + 8.5	5.5	—
32.0	2.59	0	6.5	—	6.5	11.5
		1	17	11.5	5.5	8.5
		2	25.5	11.5 + 8.5	5.5	—
42.0	2.75	0	6.5	—	6.5	11.5
		1	17	11.5	5.5	—

of the water depth D (=0.62–0.74 m) to the wavelength is 0.5. This satisfies a strict criterion for deep-sea waves (Lamb 1932). This also implies that the wind waves generated in HSWWT by LTWGM could be regarded as deep-sea waves under all laboratory conditions used in this study.

c. *Wave-generation method*

To generate wind waves using LTWGM, it is important that the power spectrum of the waves produced by the wave generator is the same as that measured. The steps for employing LTWGM are as follows:

The x-directional position of the wave-generating board $P(t)$ is controlled using the servomotor and the function generator according to the following equation:

$$P(t) = \sum_i \frac{1}{2} L_i(f_i) \sin(2\pi f_i t + \theta_i), \tag{4}$$

where $L_i(f_i)$ is the stroke length at a neutral position ($x = 0$ m) and at an arbitrary frequency f_i, t is the elapsed time, and θ_i is the random phase. Term $L_i(f_i)$ is calculated using the single summation method (Hirayama and Miyazato 2009). In this method, the energy of the waves $E_i(f_i)$ at f_i is calculated by

$$E_i(f_i) = S_{\eta\eta}(f_i)\Delta f, \tag{5}$$

where $S_{\eta\eta}(f_i)$ is the power spectrum at f_i; and Δf is the frequency width for separating $S_{\eta\eta}(f_i)$ into frequency–direction bins, which is set as 0.001 Hz. Although f_i ideally ranges from zero to infinity, an actual wave generator has lower and upper limits. Because the servomotor is not operational at frequencies greater than 3.2 Hz, the upper-frequency limit of the wave generator is taken as 3.2 Hz. A high-pass filter was used to remove the white noise in the lower-frequency region. The threshold level of the high-pass filter was set as f_{limit}, with the wave energy 0.1 times smaller than that at the peak frequency, according to the following equation:

$$E_m(f_{\text{limit}}) = \frac{1}{10} E_m(f_m) \quad (f_{\text{limit}} < f_m), \tag{6}$$

where E_m is the wave energy at f_m. The power spectrum at a frequency lower than f_{limit} is given by the wind-sea spectrum model proposed by Pierson and Moskowitz (1964), and instead of Eq. (5), the relationship between the wave energy and the power spectrum is given by the following equations:

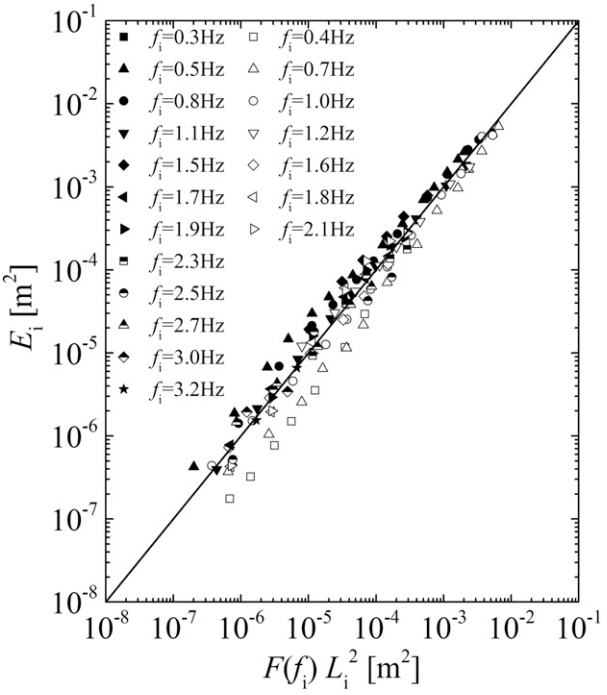

FIG. 2. Relationship between the monochromatic $E_i(f_i)$ and $L_i(f_i)$, and the empirical model for $F(f_i)$, as shown in Eqs. (13)–(15).

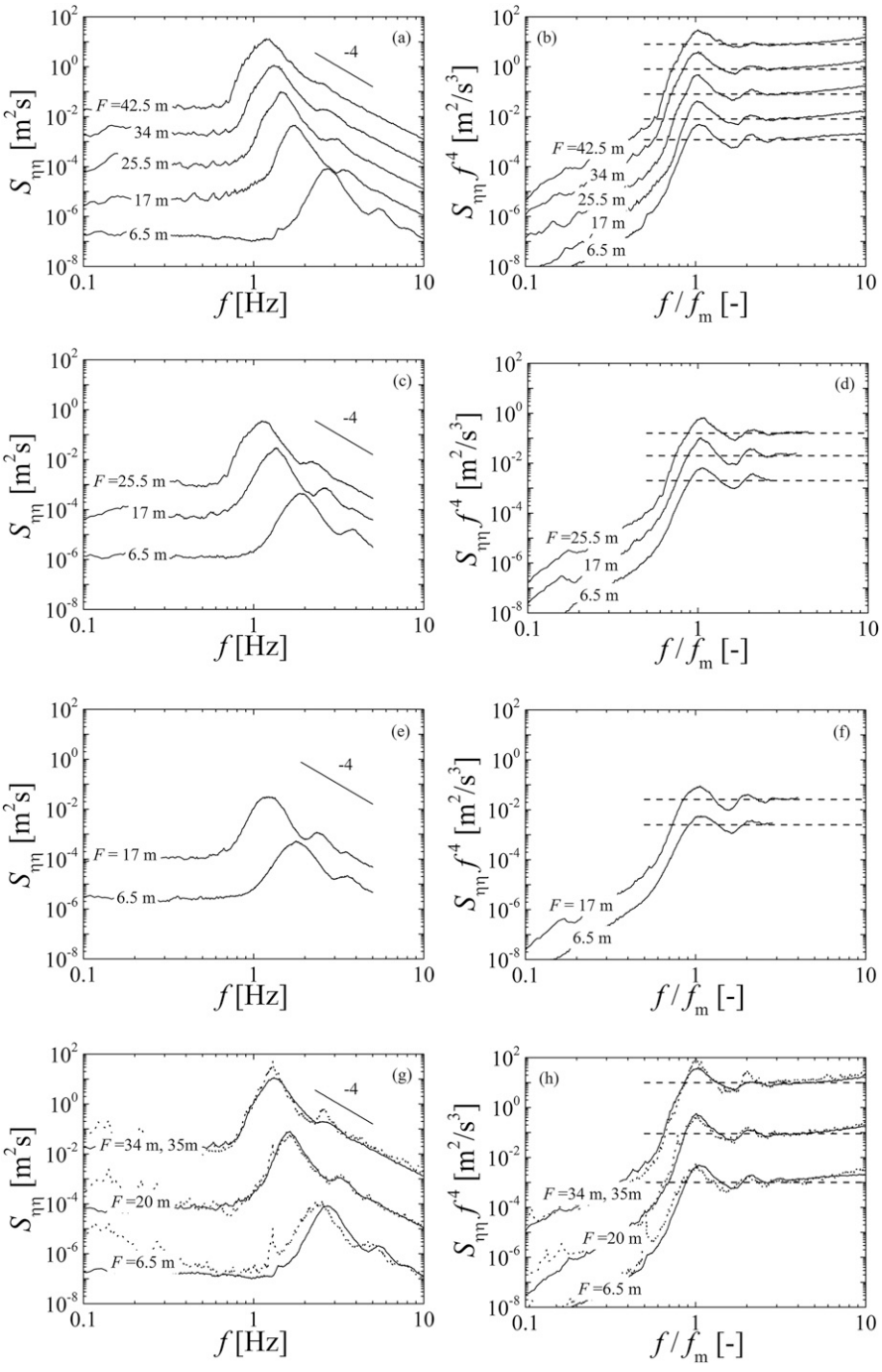

FIG. 3. Wind-sea spectra $S_{\eta\eta}$ at (a),(b) normal wind speeds (U_{10} = 19.3 m s^{-1}), (c),(d) normal wind speeds (U_{10} = 32.0 m s^{-1}), and (e),(f) extremely high wind speeds (U_{10} = 42.0 m s^{-1}); and (g),(h) comparison of wind waves generated by fan and the wave generator in HSWWT (solid curves) to those by fan in RIAM WWT (dotted curves) at normal wind speeds. Curves, from top to bottom, are for F = 42.5, 34, 25.5, 17, and 6.5 m in (a) and (b); F = 25.5, 17, and 6.5 m in (c) and (d); F = 17 and 6.5 m in (e) and (f). In (b),(d),(f), and (h), the vertical axes show spectra multiplied by the fourth power of the frequency, horizontal axes show frequencies normalized by f_m, and dotted lines show horizontal lines. Spectra at high wind speeds [(c)–(f)] are described for f = 5 Hz by removing the impingement effects of droplets and bubbles on water-level measurements (e.g., Takagaki et al. 2016a). In (g) and (h), solid curves, from top to bottom, are for F = 34, 20, and 6.5 m at U_{10} = 19.3 m s^{-1}, and dotted curves are for F = 35, 20, and 6.5 m at U_{10} = 21.7 m s^{-1}. Spectra are offset for the clarity in (a)–(h), and solid lines represent a slope of −4 in (a),(c),(e), and (g).

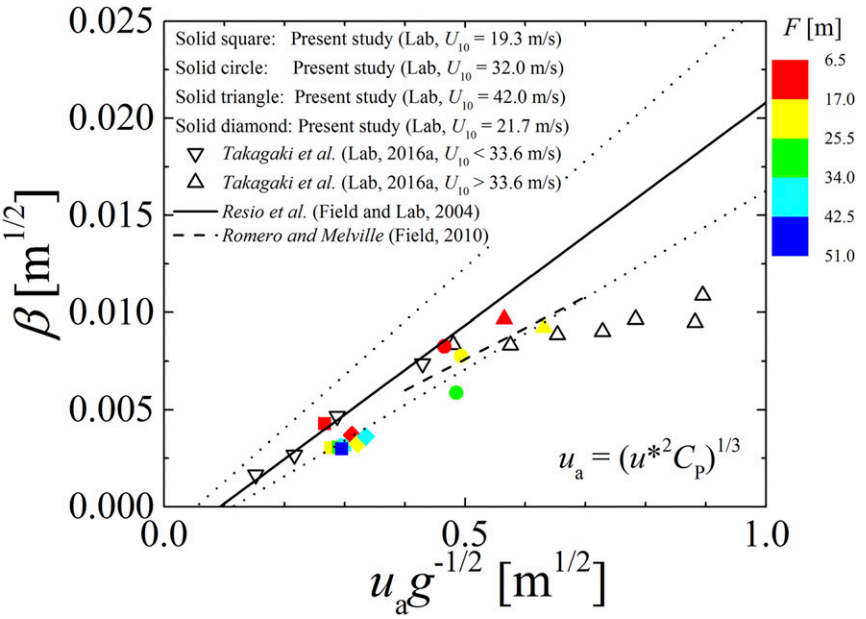

FIG. 4. Relationship between β and $u_a g^{-1/2}$. Values measured in HWWT (solid squares, circles, and triangles) and RIAM WWT (solid diamonds). Shown also are the fetch (colored bars), and the best-fit line by Resio et al. (2004; solid line), their range of values observed (dotted line), and the best-fit line by Romero and Melville (2010; dashed line).

$$E_i(f_i) = AS_{\eta\eta,\mathrm{model}}(f_i)\Delta f \quad (0\,\mathrm{Hz} < f_i < f_{\mathrm{limit}}), \tag{7}$$

$$E_i(f_i) = S_{\eta\eta,\mathrm{measured}}(f_i)\Delta f \quad (f_{\mathrm{limit}} < f_i < 3.2\,\mathrm{Hz}), \tag{8}$$

$$E_i(f_i) = 0 \quad (3.2\,\mathrm{Hz} < f_i), \tag{9}$$

where $S_{\eta\eta,\mathrm{measured}}$ is the measured power spectrum and $S_{\eta\eta,\mathrm{model}}$ is the power spectrum from the model proposed by Pierson and Moskowitz (1964):

$$S_{\eta\eta,\mathrm{model}}(f_i) = \exp\left\{-\frac{5}{4}\left(\frac{f_i}{f_m}\right)^{-4}\right\}. \tag{10}$$

The parameter A in Eq. (7) is used to connect the spectrum at $f_i = f_{\mathrm{limit}}$ and is given by

$$A = \frac{S_{\eta\eta,\mathrm{measured}}(f_{\mathrm{limit}})}{S_{\eta\eta,\mathrm{model}}(f_{\mathrm{limit}})}. \tag{11}$$

The mechanical wave generator is calibrated in advance to generate irregular waves. First, the position of the wave-generating board is fluctuated regularly according to the following equation:

$$P(t) = \frac{1}{2}L_i(f_i)\sin(2\pi f_i t + \theta_i). \tag{12}$$

The relationship between the monochromatic wave energy $E_i(f_i)$, f_i, and $L_i(f_i)$ can be expressed using the following equations:

$$E_i(f_i) = F(f_i)L_i^2(f_i), \tag{13}$$

$$F(f_i) = 3.08\times10^{-7}f_i^{3.33} \quad (0\,\mathrm{Hz} < f_i \le 1.0\,\mathrm{Hz}), \tag{14}$$

$$F(f_i) = 5.61\times10^{-7}f_i^3 - 3.28\times10^{-6}f_i^2 + 6.31\times10^{-6}f_i - 3.29\times10^{-6} \quad (1.0\,\mathrm{Hz} < f_i \le 3.2\,\mathrm{Hz}). \tag{15}$$

Here, $F(f_i)$ shows the empirical model for the frequency of the monochromatic wave. It is found that the empirical model shown as Eqs. (13)–(15) has good correlation for all monochromatic waves (see Fig. 2). The position of $P(t)$ is calculated using $L_i(f_i)$ at an arbitrary frequency from Eq. (4), and $L_i(f_i)$ is calculated from the measured wind-sea spectrum by Eqs. (7)–(9) and (13)–(15). Therefore, by controlling $P(t)$, wind waves at a fetch longer than the streamwise length of HSWWT can be generated by LTWGM.

d. *Verification experiments*

To verify the wind waves generated by LTWGM in HSWWT, we provided additional measurements in another long wind-wave tank [Research Institute for Applied Mechanics, Kyusyu University (RIAM), wind-wave tank (WWT)] with a 54-m-long test section. We measured the mean wind speed at F = 6.5, 20, and 35 m using a pitot tube and an electric differential pressure gauge (Testo 6321), and estimated U_{10} using the profile method with the log law [Eq. (2)]. The sampling frequency and the sampling time were 1 Hz and 120 s,

respectively. In addition, we measured the water-level fluctuation using custom capacitance-type wave gauges with $\Delta x = 0.15$ m for $F = 6.5$ m and at $\Delta x = 0.3$ m for $F = 20, 35$ m. The preliminarily relationship between the output voltages of the gauges and water levels were calibrated. The sampling frequency and the sampling time were 100 Hz and 360 s, respectively. The energy, peak frequency, wavelength, and phase velocity of significant wind waves were evaluated by spectral and cospectra methods, as with the case in HSWWT (see the details in section 2a). Output voltages of the differential pressure gauge and wave gauges were recorded using a digital recorder (Teac PS2032GP).

3. Results

To verify that the laboratory wind waves generated using LTWGM are similar to those observed in the ocean, we have to investigate the wind-sea spectrum shape, fetch law, dispersion relation, and Toba's 3/2 power law (Toba 1972), since these laws are observed for pure wind-driven waves in both the ocean and the laboratory. Figure 3 shows the wind-sea spectra at $U_{10} = 19.3$, 32.0, and 42.0 m s^{-1} for several fetch conditions. Here, to clarify the slope at the spectral tails, Figs. 3b,d,f show the spectra multiplied by the fourth power of the frequency against the frequencies normalized by the peak frequency. It is observed that the wind-sea spectra under long-fetch conditions consist of a single peak as a result of significant waves and spectra under short-fetch conditions, and that the peak frequency decreases with increasing the fetch. This is attributed to the development of wind waves owing to the increase in the fetch. In addition, although waves with frequencies higher than 3.5 Hz cannot be produced by the present wave generator, the slope at frequencies higher than f_m corresponds to a value of -4 in the frequency range from $f/f_m = 1.5$ to 4 (see Figs. 3b,d,f). This implies that despite the generation of mechanical irregular waves by the wave generator, the wind shear itself produces the condition of local equilibrium between the wind shear and the wind waves generated by LTWGM (Toba 1973). Therefore, it is concluded that LTWGM using the programmable irregular-wave generator can generate the ideal wind waves under long-fetch conditions. Figures 3g,h show the comparisons of spectra of waves generated by LTWGM in HSWWT to those of pure wind-generated waves by a fan in RIAM WWT. It is found that those spectra of the wind waves by LTWGM correspond approximately to those of the pure wind-driven waves, although 1) the primary spectral peak size of pure wind-generated waves by the fan in the long RIAM WWT is larger than that of the wind waves generated by LTWGM in HSWWT at a long fetch of $F = 35$ m; and 2) the secondary peak at $f = 1.2$ Hz exists just on the spectrum of the fan in RIAM WWT at a short fetch of $F = 6.5$ m. The fetch relationship for the size of the wind waves is due to the initial difference as discussed later (Fig. 3g). The second difference in the secondary peak at $f = 1.2$ Hz at $F = 6.5$ m is due to the multiple wave reflection in RIAM WWT. Although we could not remove the reflection, the problem is unrelated to the establishment of LTWGM. In addition, although the -4 slope is maintained between $f/f_m = 1.5$ and 4 in Figs. 3b,h, the slopes become more gentle than -4 over $f/f_m = 4$. This may be due to the effects of bound parasitic capillary waves with phase velocities that are close to those of peak waves (e.g., Rozenberg et al. 1999).

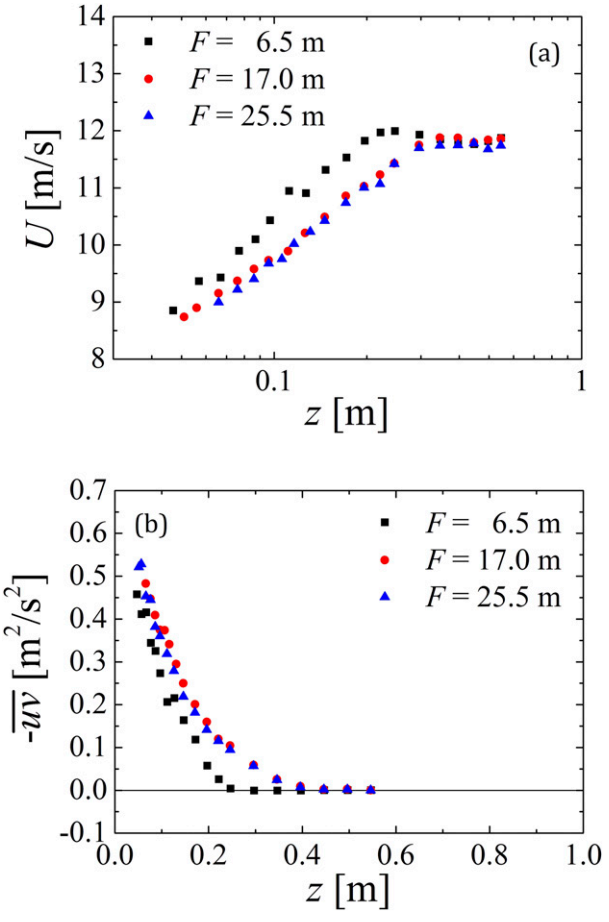

FIG. 5. Vertical distributions of (a) streamwise mean wind speed U and (b) Reynolds stress $-\overline{uv}$ at $U_{10} = 19.3$ m s^{-1}.

To quantify the spectral-tail shape, the equilibrium range constants α_R proposed by Resio et al. (2004) are evaluated. Figure 4 shows the relationship between β and $u_a g^{-1/2}$. Here, β is the coefficient relative to α_R, defined as

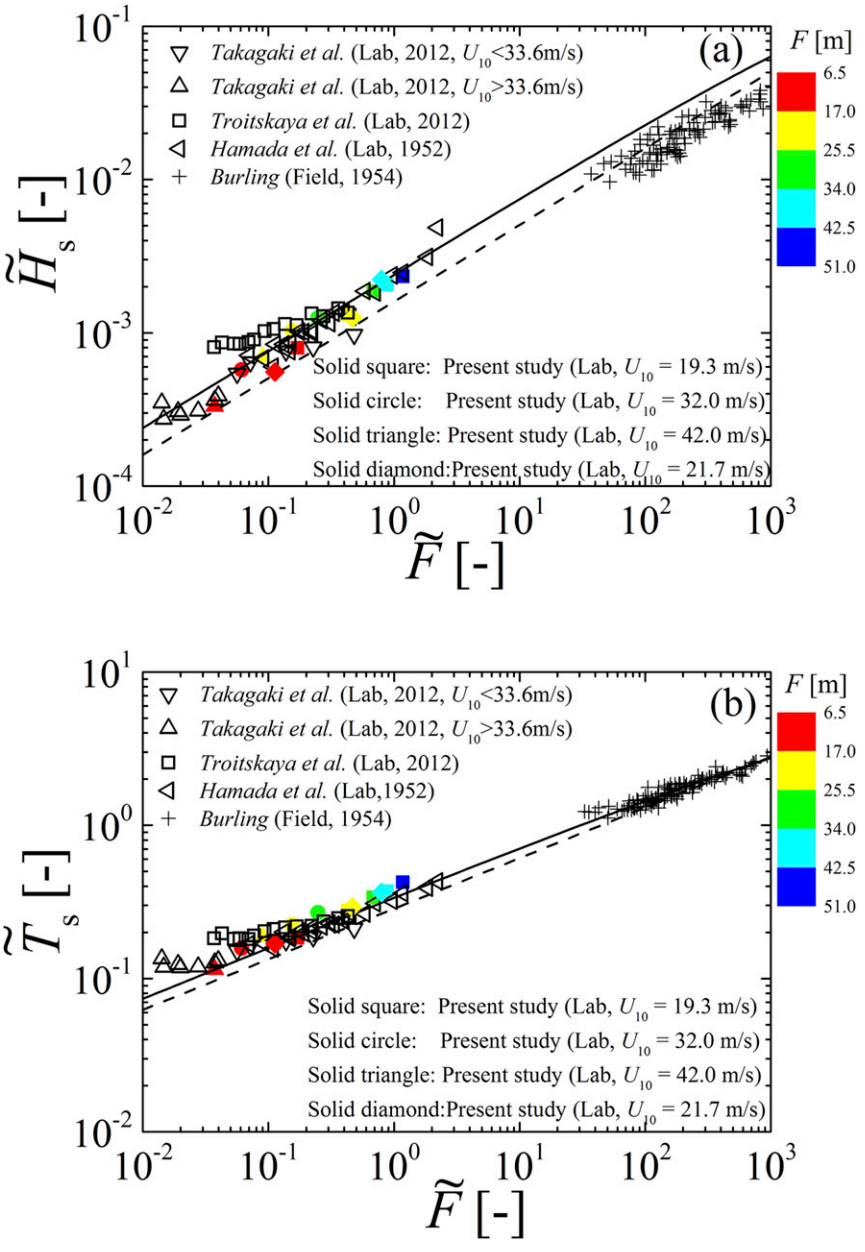

FIG. 6. Relationship between $\tilde{F}$ and (a) $\tilde{H}_S$ and (b) $\tilde{T}_S$. Fetch, wave height, and wave period are normalized using U_{10} and g. Values measured in HWWT (solid squares, circles, and triangles) and RIAM WWT (solid diamonds). Shown are Wilson's formula IV (Wilson 1965; solid curve) and JONSWAP (Hasselmann et al. 1973; dashed curve), both in (a) and (b); and fetch (colored bars). Laboratory values of Troitskaya et al. (2012) and Hamada et al. (1952) and field values of Burling (1954) are added in the figure.

$$\beta = \frac{1}{2}\alpha_R u_a g^{-1/2} - \frac{1}{2}\alpha_R u_0 g^{-1/2}, \tag{16}$$

where u_a is the velocity scale for α_R, defined as $u_a = (u^{*2}C_P)^{1/3}$, and u_0 is the small threshold velocity scale for α_R. The details for the evaluation thereof are shown in Resio et al. (2004) and are summarized in the appendix. It is clear that our values and those of Takagaki et al. (2016a) are lower than those of Resio et al. (2004), but within the range of observed values by Resio et al. (2004) at $u_a g^{-1/2} < 0.6$. In addition, our values corresponds well to those by Romero and Melville (2010) at $0.4 < u_a g^{-1/2} < 0.6$. However, α_R requires more elaborate analysis, because our values at $U_{10} > 33.6\,\mathrm{m\,s^{-1}}$ without

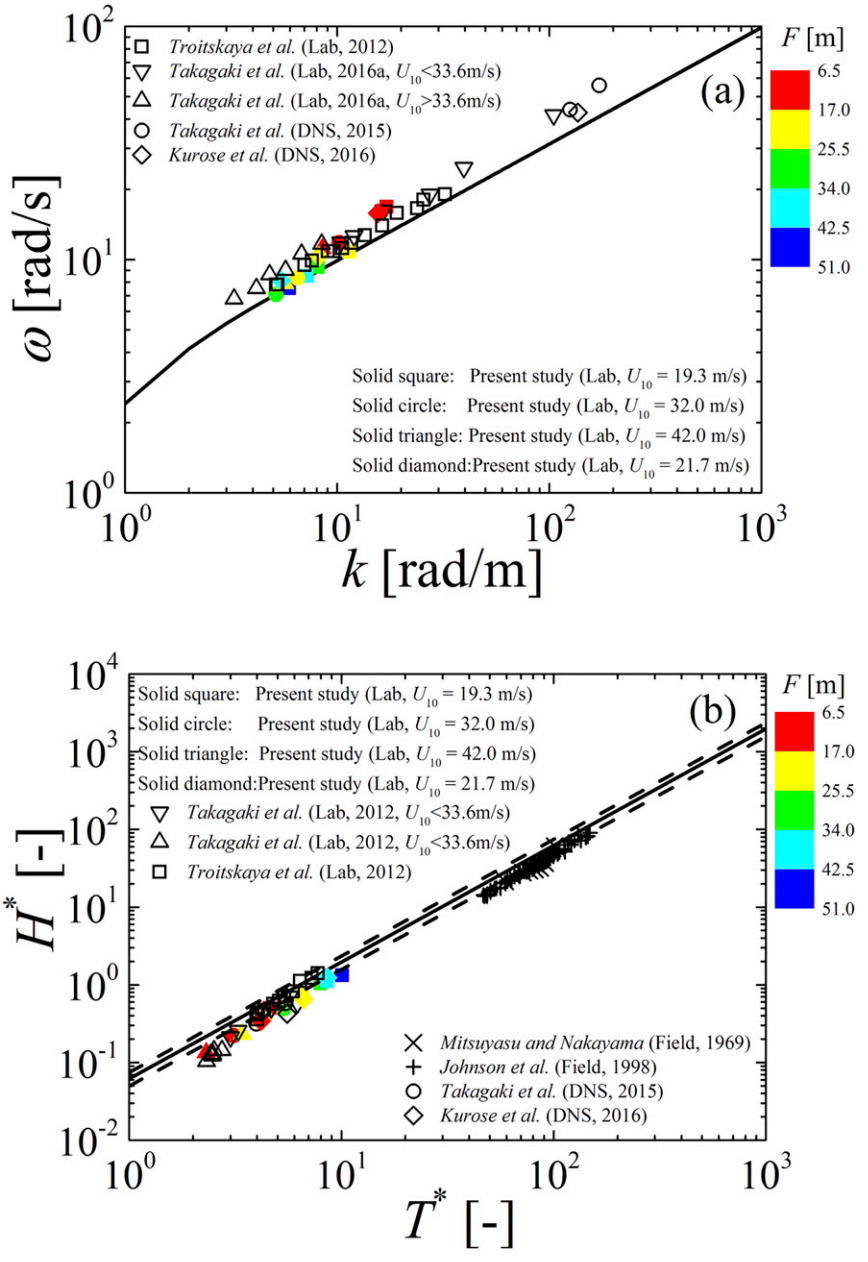

FIG. 7. (a) Dispersion relation, and (b) relationship between T^* and H^*. In (b), wave height and wave period are normalized using u^* and g. Values measured in HWWT (solid squares, circles, and triangles) and RIAM WWT (solid diamonds). In (a) and (b), the dispersion relation and Toba's 3/2 power law (Toba 1973), respectively, are shown (solid curve). In (b) the 20% errors in Toba's 3/2 power law (Toba 1973) are shown (dashed curves). The fetch is indicated (colored bars). Laboratory values of Troitskaya et al. (2012), predicted values of Takagaki et al. (2015) and Kurose et al. (2016), and field values of Mitsuyasu and Nakayama (1969) and Johnson et al. (1998) are added in the figure.

LTWGM (Takagaki et al. 2016a), shown at $0.6 < u_a g^{-1/2} < 0.9$, have large discrepancies compared to those by Resio et al. (2004). In fact, Resio et al. (2004) does not include values at $U_{10} > 33.6\,\mathrm{m\,s^{-1}}$. The results support that $u_a = (u^{*2} C_P)^{1/3}$ is a suitable velocity scale for α_R at $U_{10} < 33.6\,\mathrm{m\,s^{-1}}$.

Figure 5 shows the vertical distribution of the mean wind speed and the Reynolds stress for $F = 6.5$, 25.5, and 42.5 m at $U_{10} = 19.3\,\mathrm{m\,s^{-1}}$. Large waves generated by the wave generator may disturb an inner layer of the airflow field near the water surface by turbulent mixing due to large surface waves. However, in the figure, we can

confirm the ideal turbulent boundary airflow that has the free-stream wind region, with the zero Reynolds stress, and the log-law region, with the Reynolds stress decreasing with height z under all the fetch conditions.

Figure 6 shows that the relationships of the nondimensional fetch $\widetilde{F}(=Fg/U_{10}^2)$ to the nondimensional wave height $\widetilde{H}_S(=H_Sg/U_{10}^2)$, and to the nondimensional wave period $\widetilde{T}_S(=T_Sg/U_{10})$. Here, the solid and dashed curves represent the fetch law from Wilson's formula IV (Wilson 1965) and JONSWAP (Hasselmann et al. 1973), respectively. It is observed that the present plots under both short- and long-fetch conditions are concentrated around the solid and dashed curves, respectively, which implies that the wind waves follow the fetch law at $U_{10} < 33.6\,\mathrm{m\,s^{-1}}$. Figure 7 shows the dispersion relation and the relationship between the nondimensional wave period T^* $(= T_Sg/u^*)$ and the nondimensional wave height H^* $(= H_Sg/u^{*2})$. Here, solid curves show the dispersion relation for a deep-sea wave (Lamb 1932) in Fig. 7a and Toba's 3/2 power law (Toba 1972) in Fig. 7b. The figures show that the present plots under both short- and long-fetch conditions are concentrated around the solid curve, which implies that the wind waves could be regarded as deep-sea waves following the Toba's 3/2 power law at $U_{10} < 33.6\,\mathrm{m\,s^{-1}}$. The data obtained in RIAM WWT are also added in Figs. 6, 7. We can see that wind waves generated by LTWGM in HSWWT correspond well to those of pure wind-driven waves in RIAM WWT without LTWGM. At $U_{10} > 33.6\,\mathrm{m\,s^{-1}}$, the laboratory data in Figs. 6, 7b do not seem to follow the fetch law and Toba's 3/2 power law, although they follow the dispersion relation in Fig. 7a. Note that we cannot validate observation data at $U_{10} > 33.6\,\mathrm{m\,s^{-1}}$ on the fetch law, dispersion relation, and Toba's 3/2 power law, because we do not have any observation data at $U_{10} > 33.6\,\mathrm{m\,s^{-1}}$, because of the difficulty in observing at high wind speeds.

4. Discussion

The abovementioned verifications confirmed ideal wind-driven waves under long-fetch conditions can be generated using LTWGM with the programmable irregular-wave generator. Unfortunately, present long-fetch conditions produced in the laboratory experiments with LTWGM do not correspond perfectly to the field conditions. The differences between the present laboratory conditions and the field conditions are as follows. 1) The initial airflow entering the test section in each loop has a new turbulent boundary layer above the air–water interface under the present laboratory conditions; however, the boundary layer continues to develop under field conditions. 2) The present wave generator with LTWGM in HSWWT with a width of 0.8 m cannot produce the angular wave-sea spectrum, although the actual ocean waves spread to angular directions under field conditions. 3) The slope of the spectral tail is more gentle than -4 over $f/f_m = 4$ (see Figs. 3b,h), although the tail often maintains the -4 slopes under field conditions. These points should be improved before regarding the long-fetch laboratory conditions as ocean conditions, but the present LTWGM would be helpful in laboratory experiments for modeling of small-scale air–sea coupling by means of laboratory experiments.

Acknowledgments. This work was supported by the Ministry of Education, Culture, Sports, Science and Technology (Grants-in-Aid 25249013, 16K18015). We thank H. Muroya and S. Urakawa for their help in conducting experiments at HSWWT, Kyoto University. The authors acknowledge A. Isobe, K. Yufu, M. Ishibashi, and K. Takane for their help in conducting the laboratory measurements at RIAM WWT, Kyushu University.

APPENDIX

Equilibrium Range Constant

Resio et al. (2004) evaluated α_R by the wind-sea spectrum against the wavenumber $F(k)$:

$$F(k) = \frac{1}{2}\alpha_R[u_a - u_0]g^{-\frac{1}{2}}k^{-\frac{5}{2}} = \beta k^{-\frac{5}{2}}, \qquad \text{(A1)}$$

where u_a is the velocity scale for α_R, u_0 is the small threshold velocity scale for α_R, g is the gravity acceleration, κ is the wavenumber, and β is defined as

$$\beta = \frac{1}{2}\alpha_R u_a g^{-1/2} - \frac{1}{2}\alpha_R u_0 g^{-1/2}. \qquad \text{(A2)}$$

Using the dispersion relation, the wind-sea spectrum against the wave frequency $S(f)$ is written as

$$S(f) = \alpha_R(2\pi)^{-3}g[u_a - u_0]f^{-4} = \beta' f^{-4}, \qquad \text{(A3)}$$

where the relationship between β and β' is shown as

$$\beta = \beta'(2\pi)^3/2g^{-3/2}. \qquad \text{(A4)}$$

Resio et al. (2004) investigated the β trend on six velocity scales, which are u^*, U_{10}, u_λ, $(u^{*2}C_P)^{1/3}$, $(U_{10}^2C_P)^{1/3}$, and $(u_\lambda^2C_P)^{1/3}$. They found the velocity scale of $u_a = (u_\lambda^2C_P)^{1/3}$ has the strongest linear correlation with β, and the best-fit curve is shown as

$$\beta = au_a g^{-1/2} + b, \tag{A5}$$

and α_R and u_0 are estimated as 0.005 53 and 1.92, respectively. Here u_λ and C_P are the wind speed at an elevation that is a fraction λ of the wavelength of significant wind waves and phase velocity, respectively. The u_λ is estimated by

$$u_\lambda = \frac{u^*}{\kappa} \ln\left(\frac{z_\lambda}{z_0}\right), \tag{A6}$$

where u^* is the friction velocity; κ is the von Kármán constant; z_λ is the length defined as $z_\lambda = \lambda L_S$ with $\lambda = 0.065$ (Resio et al. 2004), where L_S is the wavelength of significant waves; and z_0 is the roughness length. In addition, they evaluated the values of $\alpha_R = 0.0459$ and $u_0 = 0.291$ in Eq. (A2) with the velocity scale of $u_a = (u^{*2}C_P)^{1/3}$, and found that the correlation coefficients are approximately the same [$r^2 = 0.934$ for $u_a = (u^{*2}C_P)^{1/3}$, and $r^2 = 0.939$ for $u_a = (u_\lambda^2 C_P)^{1/3}$].

REFERENCES

Burling, R. W., 1954: Surface waves on enclosed bodies of water. *Coastal Eng. Proc.*, **5**, 1–10, doi:10.9753/icce.v5.1.

Donelan, M. A., B. K. Haus, N. Reul, W. J. Plant, M. Stiassnie, H. C. Graber, O. B. Brown, and E. S. Saltzman, 2004: On the limiting aerodynamic roughness of the ocean in very strong winds. *Geophys. Res. Lett.*, **31**, L18306, doi:10.1029/2004GL019460.

Hamada, T., H. Mitsuyasu, and N. Hase, 1953: An experimental study of wind effect upon water surface. Rep. of Transportation Technical Research Institute 8, 22 pp.

Hasselmann, K., and Coauthors, 1973: Measurements of wind-wave growth and swell decay during the Joint North Sea Wave Project (JONSWAP). Deutschen Hydrographischen Zeitschrift Ergänzungsheft 8-12, 95 pp.

Hawkins, H. F., and D. T. Rubsam, 1968: Hurricane Hilda, 1964; II. Structure and budgets of the hurricane on October 1, 1964. *Mon. Wea. Rev.*, **96**, 617–636, doi:10.1175/1520-0493(1968)096<0617:HH>2.0.CO;2.

Hirayama, K., and I. Miyazato, 2009: Generation method of directional random waves with arbitrary spectrum. Port and Airport Research Institute Rep. 048-02-09, 119–214.

Iwano, K., N. Takagaki, R. Kurose, and S. Komori, 2013: Mass transfer velocity across the breaking air–water interface at extremely high wind speeds. *Tellus*, **65B**, 21 341, doi:10.3402/tellusb.v65i0.21341.

Johnson, H. K., J. Hojstrup, H. J. Vested, and S. E. Larsen, 1998: On the dependence of sea surface roughness on wind waves. *J. Phys. Oceanogr.*, **28**, 1702–1716, doi:10.1175/1520-0485(1998)028<1702:OTDOSS>2.0.CO;2.

Komori, S., R. Nagaosa, and Y. Murakami, 1993: Turbulence structure and mass transfer across a sheared air–water interface in wind-driven turbulence. *J. Fluid Mech.*, **249**, 161–183, doi:10.1017/S0022112093001120.

Krall, K. E., and B. Jähne, 2014: First laboratory study of air–sea gas exchange at hurricane wind speeds. *Ocean Sci.*, **10**, 257–265, doi:10.5194/os-10-257-2014.

Kunishi, H., and N. Imasato, 1966: On the growth of wind waves by high-speed wind flume (in Japanese). Kyoto University Disaster Prevention Research Institute Annuals 9, 667–676.

Kurose, R., N. Takagaki, A. Kimura, and S. Komori, 2016: Direct numerical simulation of turbulent heat transfer across a sheared wind-driven gas–liquid interface. *J. Fluid Mech.*, **804**, 646–687, doi:10.1017/jfm.2016.554.

Lamb, H., 1932: *Hydrodynamics*. 6th ed. Cambridge University Press, 738 pp.

Mitsuyasu, H., and R. Nakayama, 1969: Measurements of waves and wind at Hakata Bay. Rep. Res. Inst. Appl. Mech., 33, 33–66.

——, Y.-Y. Kuo, and A. Masuda, 1979: On the dispersion relation of random gravity waves. Part 2. An experiment. *J. Fluid Mech.*, **92**, 731–749, doi:10.1017/S0022112079000859.

Phillips, M., 1958: The equilibrium range in the spectrum of wind-generated ocean waves. *J. Fluid Mech.*, **4**, 426–434, doi:10.1017/S0022112058000550.

Pierson, W. J., and L. Moskowitz, 1964: A proposed spectral form for fully developed wind seas based on the similarity theory of S. A. Kitaigorodskii. *J. Geophys. Res.*, **69**, 5181–5190, doi:10.1029/JZ069i024p05181.

Powell, M. D., P. J. Vickery, and T. A. Reinhold, 2003: Reduced drag coefficient for high wind speeds in tropical cyclones. *Nature*, **422**, 279–283, doi:10.1038/nature01481.

Resio, D. T., C. E. Long, and C. L. Vincent, 2004: Equilibrium-range constant in wind-generated wave spectra. *J. Geophys. Res.*, **109**, C01018, doi:10.1029/2003JC001788.

Romero, L., and W. K. Melville, 2010: Airborne observations of fetch-limited waves in the Gulf of Tehuantepec. *J. Phys. Oceanogr.*, **40**, 441–465, doi:10.1175/2009JPO4127.1.

Rozenberg, A. D., W. K. Melville, M. J. Ritter, C. C. Gottschall, and A. V. Smimov, 1999: Free and bound capillary waves as microwave scatterers: Laboratory studies. *IEEE Trans. Geosci. Remote Sens.*, **37**, 1052–1065, doi:10.1109/36.752223.

Takagaki, N., and S. Komori, 2007: Effects of rainfall on mass transfer across the air-water interface. *J. Geophys. Res.*, **112**, C06006, doi:10.1029/2006JC003752.

——, ——, N. Suzuki, K. Iwano, T. Kuramoto, S. Shimada, R. Kurose, and K. Takahashi, 2012: Strong correlation between the drag coefficient and the shape of the wind sea spectrum over a broad range of wind speeds. *Geophys. Res. Lett.*, **39**, L23604, doi:10.1029/2012GL053988.

——, R. Kurose, Y. Tsujimoto, S. Komori, and K. Takahashi, 2015: Effects of turbulent eddies and Langmuir circulations on scalar transfer in a sheared wind-driven liquid flow. *Phys. Fluids*, **27**, 016603, doi:10.1063/1.4905845.

——, S. Komori, and N. Suzuki, 2016a: Estimation of friction velocity from the wind-wave spectrum at extremely high wind speeds. *IOP Conf. Series: Earth Environ. Sci.*, **35**, 012009, doi:10.1088/1755-1315/35/1/012009.

——, ——, ——, K. Iwano, and R. Kurose, 2016b: Mechanism of drag coefficient saturation at strong wind speeds. *Geophys. Res. Lett.*, **43**, 9829–9835, doi:10.1002/2016GL070666.

Toba, Y., 1972: Local balance in the air-sea boundary processes. I. On the growth processes of wind waves. *J. Oceanogr. Soc. Japan*, **28**, 109–121, doi:10.1007/BF02109772.

——, 1973: Local balance in the air-sea boundary processes. III. On the spectrum of wind waves. *J. Oceanogr. Soc. Japan*, **29**, 209–220, doi:10.1007/BF02108528.

Troitskaya, Y. I., D. A. Sergeev, A. A. Kandaurov, G. A. Baidakov, M. A. Vdovin, and V. I. Kazakov, 2012: Laboratory and theoretical modeling of air-sea momentum transfer under severe wind conditions. *J. Geophys. Res.*, **117**, C00J21, doi:10.1029/2011JC007778.

Wilson, B. W., 1965: Numerical prediction of ocean waves in the North Atlantic for December, 1959. *Dtsch. Hydrogr. Z.*, **18**, 114–130, doi:10.1007/BF02333333.